

Oxygen Vacancies Riched PrO_x Polycrystalline Nanorods on Graphene Nanosheets as Advanced Oxygen Catalysts for Lithium-Oxygen Batteries

Xingyi Zhan,^[a] Yifan Zhang,^[a] Liwei Su,*^[a, d] Lei Zhang,^[a] Zijin Tong,^[a] Hao Wu,^[a] Lianbang Wang,*^[a, d] Yuanhao Wang,*^[b] and Xiaoxiang Wang^[c]

The slow reaction kinetics of Li–O is currently the most pressing technical obstacle to the development of lithium-oxygen batteries. The Li_2O_2 's growth/decomposition pathways dominate the battery performance and can be optimized by exploring efficient cathode catalysts. Herein, we prepare regular, polycrystalline, oxygen vacancy (V_{O})-riched PrO_x uniformly anchored on few-layered graphene (FLG) nanosheets to boost the Li–O reactions. XRD, TGA, XPS, SEM, TEM, SEAD, and electrochemical test techniques are used to study their chemical composition, microstructure, battery performance, and the effect of FLG on the formation of polycrystalline and V_{O} . It is confirmed that FLG provides a large specific surface

area and good electron transport. Moreover, it works as an anchoring substrate to transform PrO_x from single crystal to polycrystalline, which is beneficial for exposing catalytic sites and V_{O} and improving the battery performance. This unique composition and structure offer efficient active sites, accelerate electron transport, and regulate the Li_2O_2 's nucleation to form nanofilms or nanosheets on the catalyst. With this cathode catalyst, the battery achieved an ultralow total overpotential of 0.618 V, with a discharge capacity of 11489 mAh g^{-1} in the ultimate-capacity mode and a superior cyclability of 85 cycles under the limited capacity of 500 mAh g^{-1} .

Introduction

Lithium-oxygen batteries (LOBs) are considered one of the most promising energy storage devices due to their high energy density comparable to gasoline. However, they are still in the early stages of laboratory exploration, and many thorny issues remain.^[1–7] The sluggish Li–O reaction kinetics is the most urgent technical barrier, including oxygen reduction reaction (ORR) and oxygen evolution reaction (OER), leading to large charge-discharge overpotentials and low round-trip

efficiency.^[8–13] In addition, the insulation of Li_2O_2 hinders electron/ion transport and significantly reduces energy efficiency and lifespan.^[14–17] Generally, the discharge capacity, rate performance, overpotential, and longevity of LOBs are determined by the quantity, morphology, accumulation behaviors, and growth and decomposition pathways of Li_2O_2 .^[18,19] Peng et al.^[20] demonstrated that the reaction interface of LOBs is electrode/ Li_2O_2 rather than Li_2O_2 /electrolyte. Therefore, developing an efficient catalyst to increase the effective contact sites between the electrode surface and Li_2O_2 is crucial to optimizing the reaction path and regulating Li_2O_2 nucleation.

Among cubic fluorite materials,^[21–24] Pr_6O_{11} has many advantages in the catalyst field.^[25,26] The electron hopping between Pr^{3+} and Pr^{4+} endows Pr_6O_{11} with high electronic conductivity.^[27,28] Due to the shielding of 5 s electrons in the outer layer, 4f electrons in Pr exhibit localization and incomplete filling, making it easier to change their valence states and possess unique redox capabilities.^[29,30] Our previous work introduced Pr_6O_{11} as an efficient cathode catalyst for LOBs for the first time and found that regulating the temperature-dependent oxygen vacancy (V_{O}) concentration could greatly affect its catalytic performance in the Li–O reactions. Although V_{O} causes Pr_6O_{11} to deviate from its stoichiometric ratio, it does not destroy its cubic fluorite crystal structure; instead, it provides additional catalytic active sites, good conductivity, and fast reaction kinetics. This material optimized the reaction pathway with metal-like $\text{Li}_{2-x}\text{O}_2$ and adjusted Li_2O_2 into vertically staggered nanosheets, effectively avoiding the suffocation on the catalyst surface, thus exhibiting good capacity, cyclic stability, and rate performance.^[31] However, severe aggregation of V_{O} -rich Pr_6O_{11} nanocrystals resulted in insufficient exposure

[a] X. Zhan, Y. Zhang, Prof. Dr. L. Su, L. Zhang, Z. Tong, H. Wu, Prof. Dr. L. Wang
State Key Laboratory Breeding Base of Green Chemistry-Synthesis Technology,

College of Chemical Engineering,
Zhejiang University of Technology,
Hangzhou 310014, P. R. China
E-mail: wanglb99@zjut.edu.cn
suliwei@zjut.edu.cn

[b] Prof. Dr. Y. Wang
Hoffmann Institute of Advanced Materials,
Shenzhen Polytechnic,
Shenzhen 518055, P. R. China
E-mail: wangyuanhao@szpt.edu.cn

[c] Dr. X. Wang
Anteotech, Queensland 4113, Australia

[d] Prof. Dr. L. Su, Prof. Dr. L. Wang
Key Laboratory of the Ministry of Education for Advanced Catalysis Materials,
Zhejiang Normal University,
Jinhua 321004, China

 Supporting information for this article is available on the WWW under <https://doi.org/10.1002/batt.202300479>

to oxygen-deficient catalytic sites and greatly reduced the effective reaction area, thereby limiting battery performance to a great extent.

Based on the above considerations, this work employed a hydrothermal method to prepare ultrafine (20–40 nm in diameter) and ultrashort (100–300 nm in length) PrOOH nanorods (NRs) onto few-layered graphene (FLG) nanosheets. A high-temperature calcination was used to convert PrOOH into a high-V_O-concentration polycrystalline PrO_x. The existence of FLG could homogeneously disperse PrO_x and, more importantly, induce the formation of polycrystalline.

Results and Discussion

Characterization of Materials

Figure 1a schematically shows the two-step preparation process of the PrO_x@FLG composite. (1) FLG nanosheets worked as a Pr³⁺ captor to *in-situ* form PrOOH NRs during hydrothermal. (2) The PrOOH NRs on FLG further decomposed into high-V_O Pure PrO_x during calcination. Figures 1b–d show the uniform distri-

bution of Pure PrO_x on the FLG nanosheets. As shown in the TEM image (Figure 1c), PrO_x has a regular shape of NRs (20–40 nm in diameter and 100–300 nm in length). The EDS mapping (Figure 1d) exhibits the uniform distribution of O and Pr in NRs on the carbon-based carrier. HRTEM images (Figures 1e–f) present the polycrystalline nature of PrO_x in PrO_x@FLG. There are many microcrystals (<5 nm in diameter) piled up in the NRs disorderly (Figure 1f, S1). The lattice spacing of 0.283 and 0.323 nm are indexed to the (111) and (200) planes of fluorite Pr₆O₁₁, respectively. Moreover, point defects can be observed. The SAED patterns (Figure 1g) further confirm the polycrystalline nature of Pure PrO_x, and the diffraction rings correspond to the (111), (200), (220), and (311) planes of fluorite Pr₆O₁₁. Low-magnification TEM images (Figure S2) show further the uniformity of Pure PrO_x and PrO_x-FLG.

It is worth noting that the FLG nanosheets play a crucial role in the homogeneous dispersion and polycrystalline formation of Pure PrO_x. Without FLG nanosheets in the hydrothermal, Pure PrO_x (Figure S3a–c) and PrO_x-FLG (Figure S4a–c) agglomerate into a rod-stacked structure during the high-temperature calcination. More importantly, the Pure PrO_x in these two samples is a single crystal (Figure S3d, S4d). The

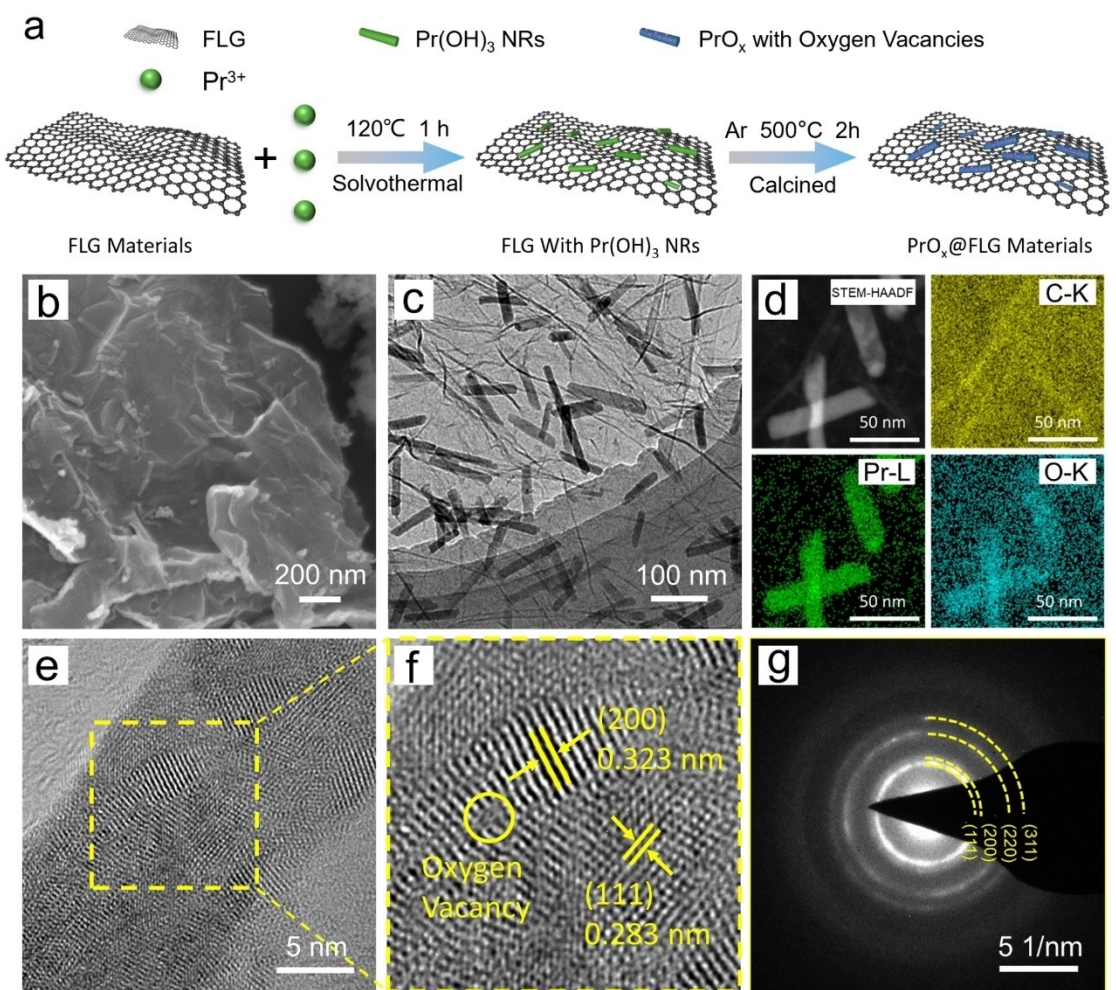


Figure 1. (a) Schematic diagram of the preparation of PrO_x@FLG; (b) SEM, (c) TEM, (d) mapping, (e) HRTEM, (f) corresponding lattice fringes, and (g) SAED images.

homogeneous dispersion and polycrystalline formation of Pure PrO_x are due to the *in-situ* growth of PrOOH precursors on the FLG surface, significantly inhibiting Pure PrO_x aggregation while exhibiting a regular morphology.

XRD, TGA, N_2 adsorption/desorption, and XPS techniques were carried out to determine the chemical composition of the three samples. As shown in Figure 2a, the XRD diffraction peaks of all samples correspond well to cubic fluorite Pr_6O_{11} (JCPDS No. 00-042-1121). The main peaks at 28.3° , 32.7° , 47.0° , and 55.7° correspond to the (111), (200), (220), and (311) planes, respectively.^[32,33] TGA (Figure 2b) suggests that the carbon contents in $\text{PrO}_x@\text{FLG}$ and $\text{PrO}_x\text{-FLG}$ are 24.29% and 25.11%, respectively.

The N_2 (de)adsorption curves (Figure 2c) of all three samples are classified as Type III, with a concave isotherm and no inflection point, indicating a weak interaction force. Calculated through BET theory, the specific surface areas of Pure PrO_x , $\text{PrO}_x\text{-FLG}$, and $\text{PrO}_x@\text{FLG}$ are 74.10, 269.83, and $121.88 \text{ m}^2 \text{ g}^{-1}$, respectively. Compared to Pure PrO_x , the FLG in $\text{PrO}_x\text{-FLG}$ and $\text{PrO}_x@\text{FLG}$ offers a larger specific surface area to contact the electrolyte and a better electronic transport network.

In the Pr 3d XPS spectra (Figure 2d), the 933.9 and 954.3 eV peaks belong to Pr^{4+} , while the 929.5 and 949.4 eV peaks belong to Pr^{3+} .^[34-36] Based on the peak areas of Pr^{4+} and Pr^{3+} , the x values of PrO_x in the Pure PrO_x , $\text{PrO}_x\text{-FLG}$, and $\text{PrO}_x@\text{FLG}$ are 1.824, 1.818, and 1.776, respectively. The O 1s XPS spectra (Figure 2e) show that O exists in different chemical environments. The peaks O1 (529 eV), O2 (531.6 eV), O3 (533.3 eV), and O4 (534.4 eV) correspond to lattice oxygen, oxygen defects, hydroxyl groups, and oxygen-containing functional groups, respectively.^[34,37,38] Based on the peak areas, the ratios of oxygen defects to lattice oxygen in Pure PrO_x , $\text{PrO}_x\text{-FLG}$, and $\text{PrO}_x@\text{FLG}$ are 1.643, 2.154, and 2.747, respectively, which are consistent with the Pr^{3+} content change in the three samples. It is confirmed that $\text{PrO}_x@\text{FLG}$ has the highest V_O concentration. The

uniform distribution and polycrystalline nature of Pure PrO_x on the FLG nanosheet effectively provide more V_O active sites.

Electrochemical performance and morphology evolution during cycling

Figure 3a shows the ultimate-capacity test of the samples at a current density of 100 mA g^{-1} . The ultimate discharge capacities of Pure PrO_x , $\text{PrO}_x\text{-FLG}$, and $\text{PrO}_x@\text{FLG}$ are 3396, 7819, and 11489 mAh g^{-1} , respectively, while their ORR/OER overpotentials are $0.25/1.47 \text{ V}$, $0.23/1.46 \text{ V}$, and $0.20/1.40 \text{ V}$, respectively. $\text{PrO}_x@\text{FLG}$ shows excellent ORR/OER catalytic activity and the smallest charge-discharge voltage gap of only 1.60 V . In addition, coulombic efficiency is another important indicator for the ORR/OER catalytic activity. The coulombic efficiencies of Pure PrO_x , $\text{PrO}_x\text{-FLG}$, and $\text{PrO}_x@\text{FLG}$ are 96.94%, 103.80%, and 103.99%, respectively.

Figure 3b presents the ultimate-capacity performance of $\text{PrO}_x@\text{FLG}$ at different rates. When the current density increases to 200 and 300 mA g^{-1} , the charge-discharge overpotential increases are very small, and the capacities remain at 8867 and 6402 mAh g^{-1} , respectively. The CV profiles (Figure 3c) and EIS (Figure S5) spectra can confirm the catalytic advantage of $\text{PrO}_x@\text{FLG}$. Compared to Pure PrO_x and $\text{PrO}_x\text{-FLG}$, the $\text{PrO}_x@\text{FLG}$ has a smaller redox potential difference, larger peak currents, and higher electronic conductivity due to their unique structural advantage.

The limited-capacity testing was used to evaluate the cycling performance of the three samples. When the capacity is limited to 500 mAh g^{-1} , the initial charge-discharge overpotentials of Pure PrO_x , $\text{PrO}_x\text{-FLG}$, and $\text{PrO}_x@\text{FLG}$ are 1.739 , 1.062 , and 0.618 V , respectively (Figure 3d and S6a-b), and the batteries stop working after 23, 44, and 85 cycles, respectively. As the limited capacity to 1000 mAh g^{-1} , the $\text{PrO}_x@\text{FLG}$ maintains a

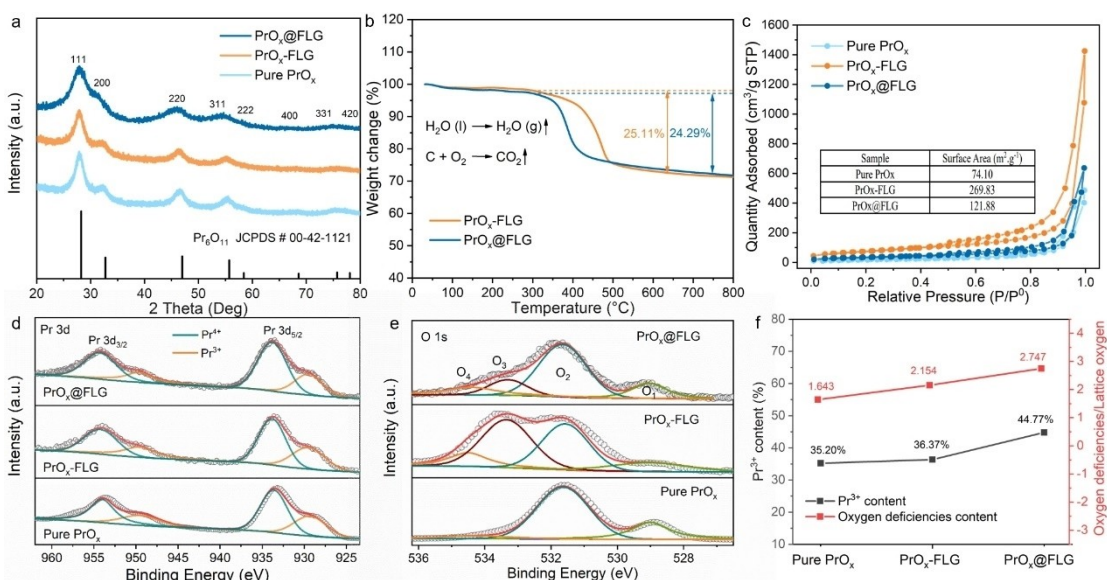


Figure 2. (a) XRD patterns, (b) TGA curves in Air, (c) N_2 adsorption and desorption curves, (d) Pr 3d XPS spectra, (e) O1s XPS spectra, and (f) Pr^{3+} content and V_O concentration of Pure PrO_x , $\text{PrO}_x\text{-FLG}$, and $\text{PrO}_x@\text{FLG}$.

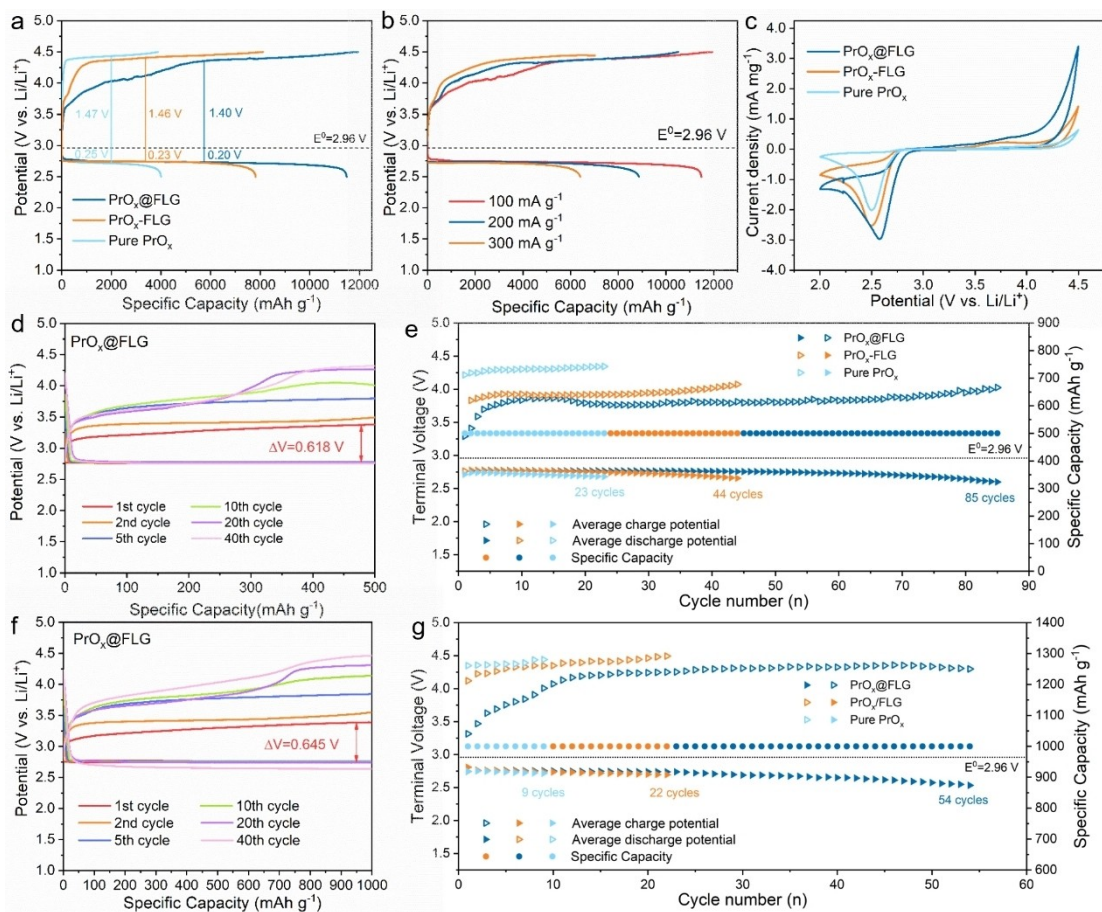


Figure 3. The ultimate-capacity charge/discharge curves of (a) the three samples at 100 mA g⁻¹ and (b) PrO_x@FLG at different rates; (c) CV profiles of the three samples. The limited-capacity performance: discharge/charge curves of PrO_x@FLG with the limited capacity of (d) 500 mA h g⁻¹ at the current density of 100 mA g⁻¹ and (f) 1000 mA h g⁻¹ at 200 mA g⁻¹; cycling performances of the three samples at the limited capacity of (e) 500 mA h g⁻¹ and (g) 1000 mA h g⁻¹.

Coulombic efficiency of ~100% for 54 cycles (Figure 3f). In contrast, Pure PrO_x and PrO_x-FLG reach the cut-off voltage after only 9 and 22 cycles, respectively (Figures 3g and S7a–b). The performance of pure FLG is shown in Figure S8.

Figure 4 shows the SEM images of PrO_x@FLG and Pure PrO_x electrode surfaces to study the morphology evolution of Li₂O₂ before and after cycling. After discharge, many Li₂O₂ nanofilms and a few nanosheets form and uniformly deposit on PrO_x@FLG surfaces (Figures 4a, b), which completely disappears after the charge (Figure 4c). In contrast, on the surface of Pure PrO_x, Li₂O₂ deposits a large flower-like morphology after discharge (Figures 4d, e), and a small amount of flower clusters remain after the charge. This strong comparison indicates that PrO_x@FLG has significantly improved the catalytic performance of both ORR and OER. Its active site can more effectively regulate the Li₂O₂'s nucleation to form thin nanofilms and nanosheets, facilitating the efficient transport of O₂ and electrolytes and significantly improving the deposition and decomposition of Li₂O₂.

XPS and EIS were used to explore further the superior performance of PrO_x@FLG during cycling. Figure 5a shows the Li 1s spectra of electrodes in different states. The characteristic peak (55.2 eV) of Li₂O₂ appears after the initial discharge and completely disappears after the charge. Figure 5b shows a

significant change in the charge transfer impedance (R_{ct}) of the PrO_x@FLG electrode before and after cycling. The initial R_{ct} is 87.9 Ω, which rapidly increases to 317.4 Ω after the discharge due to the accumulation of discharge product Li₂O₂ on the electrode surface. After charging, the R_{ct} recovers to 99.3 Ω, close to its initial value, suggesting that Li₂O₂ completely decomposes during the charging process. Both the XPS and EIS results indicate that PrO_x@FLG has good catalytic performance for the formation and decomposition of Li₂O₂.

The good performance of PrO_x@FLG can be ascribed to its unique composition and structure advantages: regular NRs, versatile FLG, and high-V_O polycrystalline PrO_x. (1) In comparison with Pure PrO_x and PrO_x-FLG, PrO_x@FLG has ultrasmall PrO_x particle sizes (30–50 nm in diameter) and much better dispersion on the conductive substrate, giving more exposed catalytic sites and better reaction kinetics. (2) FLG provides a large specific surface area and good electron transport, conducive to the uniform dispersion of PrO_x and the efficient deposition/decomposition of Li₂O₂. (3) Compared with Pure PrO_x and PrO_x-FLG, PrO_x@FLG has polycrystalline PrO_x NRs, beneficial for introducing higher V_O concentrations and exposing catalytic sites of PrO_x. These aspects optimize the Li₂O₂'s

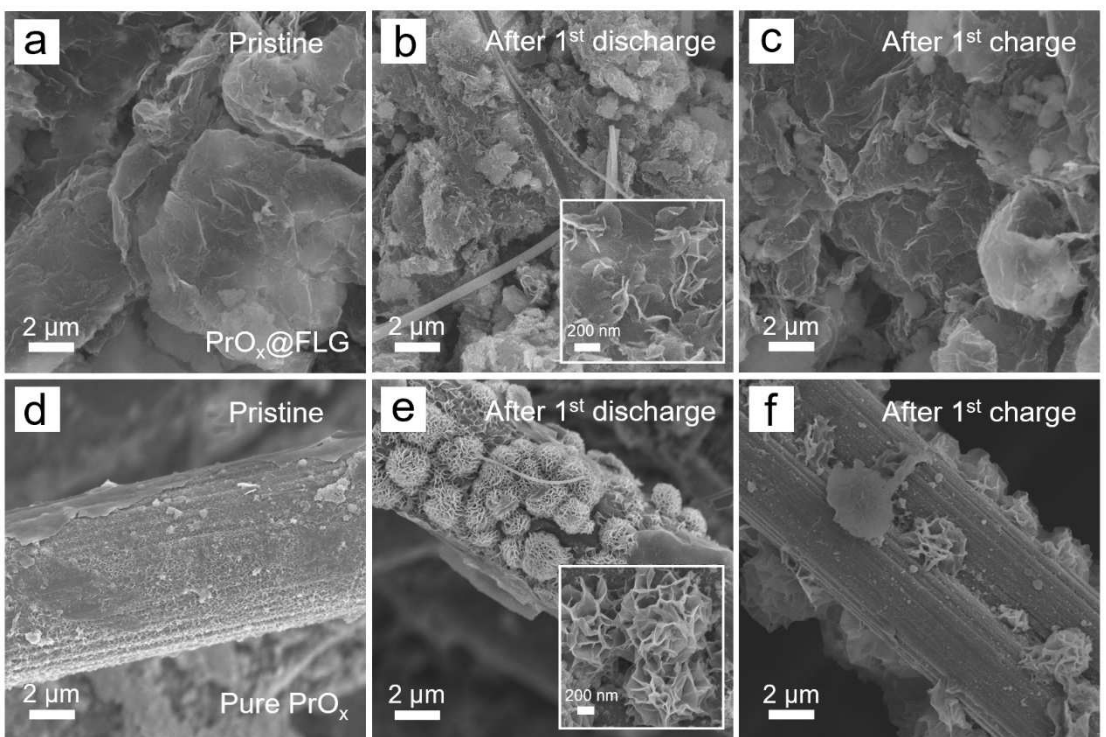


Figure 4. SEM images of $\text{PrO}_x@\text{FLG}$ and Pure PrO_x cathodes at the limited capacity of 1000 mAh g^{-1} : (a, d) pristine; (b, e) after 1st discharge; (c, f) after 1st charge.

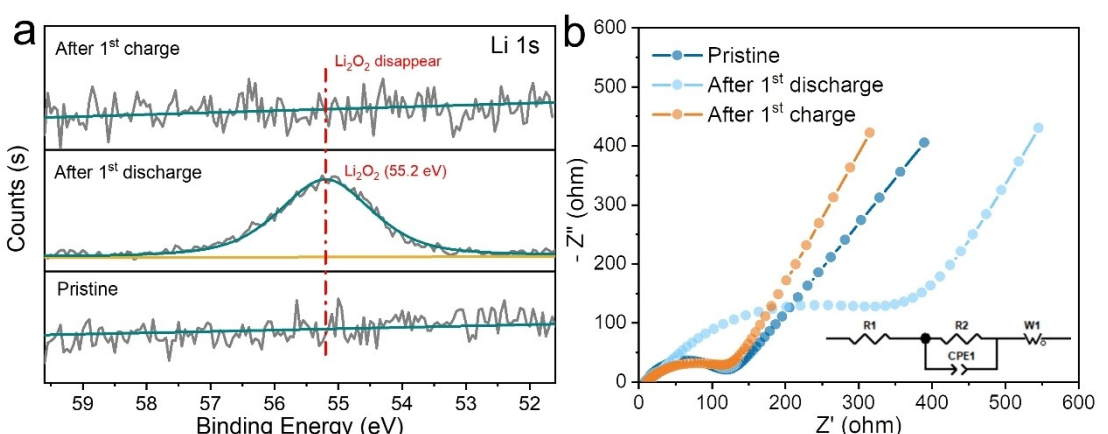


Figure 5. (a) Li 1s XPS and (b) EIS spectra of the $\text{PrO}_x@\text{FLG}$ cathode at different states.

nucleation to form uniform ultra-thin nanofilms and nanosheets, effectively preventing catalyst surface passivation.

Conclusions

Regular, polycrystalline, and V_0 -riched Pr_6O_{11} NRs (20–40 nm in diameter) were uniformly anchored on the FLG nanosheets to boost the catalytic performance in LOBs. FLG nanosheets offered a large specific surface area and good electronic conductivity. Moreover, FLG worked as an anchoring substrate to transform Pr_6O_{11} from single crystal to polycrystalline,

conducive to exposing catalytic sites and V_0 . This unique composition and structure provided efficient active sites, accelerated electron transport, and regulated the Li_2O_2 's nucleation to form nanofilms or nanosheets on the catalyst. With this cathode catalyst, the battery achieved an ultralow total overpotential of 0.618 V, with a discharge capacity of 11489 mAh g^{-1} in the ultimate-capacity mode and a superior cyclability of 85 cycles under the limited capacity of 500 mAh g^{-1} . This low-cost and efficient catalyst provides a reliable solution to the bottleneck of current LOBs and can be expanded to other ORR/OER systems.

Experimental

Preparation of Pure PrO_x and two types of PrO_x/FLG composites

All three samples were prepared through the same hydrothermal treatment and high-temperature calcination. Besides, the sources and specifications of drugs involved in the experiment are as follows: (1) Commercial Pr(NO₃)₃·6H₂O (Aladdin, 99.9%); (2) FLG nanosheets(XFNANO,0.5~5 μm,0.8 nm); (3) Urea CH₄N₂O (Aladdin, 99.5%). The differences are just whether adding FLG or not and its adding types.

Pure PrO_x: Pr(NO₃)₃·6H₂O was dissolved in 1:1 (v:v) water/ethanol to form a 20 mM solution. Then, 0.5 g urea was dispersed in 30 mL of the prepared solution, followed by adjusting the pH to 8–9 with 1 M NaOH dropwise. The solution was stirred for 30 min, sonicated for 30 min, transferred into a 50 mL Teflon-lined hydrothermal reactor, sealed, and placed in an oven at 120 °C for 1 h. After cooling to room temperature, the product (PrOOH) was washed with deionized water and ethanol (three times each) to remove Na⁺ and NO₃⁻, centrifuged, and dried at 80 °C for 12 h. Finally, the dried product was calcined at 500 °C for 2 h at a heating rate of 5 °C/min in an Ar atmosphere to obtain Pure PrO_x.

Two types of PrO_x/FLG composites: There are two types of adding FLG. One is adding 30 mg FLG to the hydrothermal solution. In this case, PrOOH NRs could in-situ form on the FLG surface during hydrothermal. The calcinated product was denoted as PrO_x@FLG. The preparation process of PrO_x@FLG is shown in Figure 1a. The other is simply mixing 30 mg FLG with the hydrothermal product PrOOH before calcination. The calcinated product was denoted as PrO_x-FLG.

Material Characterizations

X-ray diffraction (XRD, PANalytical X'Pert Pro X-ray with Cu K α radiation, $\lambda=1.5418 \text{ \AA}$, scanning rate: 2° min⁻¹), X-ray photoelectron spectroscopy (XPS, Kratos Axis DLD spectrometer with monochromatic Al K α radiation, $h\nu=1486.6 \text{ eV}$) and thermogravimetric analysis (TGA) were used to analyze the composition of the samples. Scanning electron microscopy (SEM, Hitachi S-4700 at 15 kV), transmission electron microscopy (TEM, Tecnai G2 F30 S-Twin), selected area electron diffraction (SAED), and high-resolution transmission electron microscopy (HRTEM) were adopted to study of the structure and morphology.

Electrochemical Measurements

CR2032 coin cells were assembled in a glove box filled with high-purity Ar (H₂O and O₂ < 1 ppm), using Li foil (China Energy Lithium Industry Co., Ltd.) as the counter and reference electrodes and glass fiber (Whatman GF/D) as the diaphragm. For the cathode preparation, the catalyst materials and polyvinylidene fluoride (PVDF) (9:1 w/w) were uniformly dispersed in N-methyl-2-pyrrolidone (NMP) to obtain a slurry. The slurry was drop-coated onto the surface of carbon paper (0.1 mm thick, HCP010 N, Shanghai Hesen Electric Co., Ltd., China) and vacuum-dried at 120 °C. The mass loading of active material was ~0.5 mg cm⁻². The electrolyte was dimethyl sulfoxide (DMSO) containing 1 M LiTFSI. CR2032 coin cells were placed in a sealed glass bottle for testing. The galvanostatic charge and discharge tests were carried out by the LAND test system (CT2001 A). A CHI660B workstation performed the cyclic voltammetry (CV) at 0.1 mVs⁻¹ and electrochemical impedance spectroscopy (EIS) analysis in the frequency range from 0.01 Hz to 100 kHz with an amplitude of 5 mV.

Acknowledgements

This work was supported by the National Natural Science Foundation of China (22179118 and 22075251), the Natural Science Foundation of Zhejiang Province (LGG22B030004 and LGG22E020005), and the Financial Support by Open Research Fund of Key Laboratory of the Ministry of Education for Advanced Catalysis Materials and Zhejiang Key Laboratory for Reactive Chemistry on Solid Surfaces, Zhejiang Normal University.

Conflict of Interests

The authors declare no conflict of interest.

Data Availability Statement

The data supporting this study's findings are available to the corresponding author upon reasonable request.

Keywords: praseodymium oxide · graphene · oxygen defects · synergistic effects

- [1] P. G. Bruce, S. A. Freunberger, L. J. Hardwick, J. M. Tarascon, *Nat. Mater.* **2012**, *11*, 19–29.
- [2] P. Zhang, Y. Zhao, X. B. Zhang, *Chem. Soc. Rev.* **2018**, *47*, 2921–3004.
- [3] G. Girishkumar, B. McCloskey, A. C. Luntz, S. Swanson, W. Wilcke, *J. Phys. Chem. Lett.* **2010**, *1*, 2193–2203.
- [4] Z. Zhang, L. Su, M. Yang, M. Hu, J. Bao, J. Wei, Z. Zhou, *Chem. Commun.* **2014**, *50*, 776–778.
- [5] L. L. Liu, C. C. Zhou, W. W. Fang, Y. Y. Hou, Y. P. Wu, *Energy Mater.* **2023**, *3*, 1–10.
- [6] Y. Y. Dou, D. X. Kan, Y. W. Su, Y. T. Zhang, Y. J. Wei, Z. Zhang, Z. Zhou, *J. Phys. Chem. Lett.* **2022**, *13*, 7081–7086.
- [7] M. Li, K. Pan, W. Wang, S. Xing, Y. Dou, Z. Zhang, Z. Zhou, *Batteries & Supercaps* **2023**, *6*, e202300230.
- [8] C. Z. Shu, J. Z. Wang, J. P. Long, H. K. Liu, S. X. Dou, *Adv. Mater.* **2019**, *31*, 1804587–1804629.
- [9] X. Wu, Y. Zhang, S. Chen, X. Zhan, H. Zhang, L. Zhang, L. Su, C. Shen, H. Chen, H. Wu, L. Wang, *J. Alloys Compd.* **2022**, *924*, 166354–166361.
- [10] Y. Wang, Y. Sun, W. Ren, D. Zhang, Y. Yang, J. Yang, J. Wang, X. Zeng, Y. NuLi, *Energy Mater.* **2022**, *2*, 1–29.
- [11] D. Wang, X. W. Mu, P. He, H. S. Zhou, *Mater. Today* **2019**, *26*, 87–99.
- [12] K. C. Pan, M. H. Li, W. C. Wang, S. C. Xing, Y. Y. Dou, S. S. Gao, Z. Zhang, Z. Zhou, *Green Energy & Environ.* **2023**, *8*, 939–944.
- [13] Z. Zhang, L. Zhao, Z. Xie, Z. Zhou, *Green Chem. Eng.* **2020**, *1*, 79–81.
- [14] M. D. Radin, J. F. Rodriguez, F. Tian, D. J. Siegel, *J. Am. Chem. Soc.* **2012**, *134*, 1093–1103.
- [15] O. Gerbig, R. Merkle, J. Maier, *Adv. Mater.* **2013**, *25*, 3129–3133.
- [16] D. Li, L. Zhao, J. Wang, C. Yang, *Adv. Energy Mater.* **2023**, *13*, 2204057–2204064.
- [17] V. Viswanathan, K. S. Thygesen, J. S. Hummelshøj, J. K. Nørskov, G. Girishkumar, B. D. McCloskey, A. C. Luntz, *J. Chem. Phys.* **2011**, *135*, 214704–214713.
- [18] L. Wang, S. Chen, J. Hei, R. Gao, L. Liu, L. Su, G. Li, Z. Chen, *Nano Energy* **2020**, *71*, 104570–104578.
- [19] L. N. Song, L. C. Zou, X. X. Wang, N. Luo, J. J. Xu, J. H. Yu, *iScience* **2019**, *14*, 36–46.
- [20] J. W. Wang, Y. L. Zhang, L. M. Guo, E. K. Wang, Z. Q. Peng, *Angew. Chem. Int. Ed.* **2016**, *55*, 5201–5205.
- [21] X. Yi, X. Liu, B. Qin, X. Zhao, K. W. Leong, W. Pan, K. Jiang, S. Ma, Z. Hao, D. Y. C. Leung, Z. Wen, *Mater. Today Chem.* **2023**, *29*, 101430–101441.
- [22] W. Y. Liu, Q. M. Su, L. T. Yu, G. H. Du, C. X. Li, M. Zhang, S. K. Ding, B. S. Xu, *J. Alloys Compd.* **2021**, *886*, 161189–161196.

- [23] J. J. Ge, G. H. Du, A. Kalam, X. Bi, S. K. Ding, Q. M. Su, B. S. Xu, A. G. Al-Sehemi, *Ceram. Int.* **2021**, *47*, 6965–6971.
- [24] D. Y. Li, L. L. Zhao, J. Wang, C. P. Yang, *Adv. Energy Mater.* **2023**, *13*, 2204057–2204064.
- [25] B. M. Abu-Zied, Y. A. Mohamed, A. M. Asiri, *J. Rare Earth* **2013**, *31*, 701–708.
- [26] B. L. Treu, W. G. Fahrenholtz, M. J. O'Keefe, *Inorg. Mater.* **2011**, *47*, 974–978.
- [27] B. M. Abu-Zied, *Appl. Surf. Sci.* **2019**, *471*, 246–255.
- [28] A. Netz, W. F. Chu, V. Thangadurai, R. A. Huggins, W. Weppner, *Ionics* **1999**, *5*, 426–433.
- [29] P. Sonström, J. Birkenstock, Y. Borchert, L. Schilinsky, P. Behrend, K. Gries, K. Müller, A. Rosenauer, M. Bäumer, *ChemCatChem* **2010**, *2*, 694–704.
- [30] L. Y. Wang, X. H. Yu, Y. C. Wei, J. Liu, Z. Zhao, *J. Rare Earth* **2021**, *39*, 1151–1180.
- [31] L. W. Su, Y. F. Zhang, X. Y. Zhan, L. Zhang, Y. Z. Zhao, X. L. Zhu, H. Wu, H. Chen, C. Q. Shen, L. B. Wang, *ACS Appl. Mater. Interfaces* **2022**, *14*, 40975–40984.
- [32] Y. Borchert, P. Sonström, M. Wilhelm, H. Borchert, M. Bäumer, *J. Phys. Chem. C* **2008**, *112*, 3054–3063.
- [33] N. K. Chandar, R. Jayavel, *Mater. Res. Bull.* **2014**, *50*, 417–420.
- [34] C. X. Wang, D. Z. Ren, G. Harle, Q. G. Qin, L. Guo, T. T. Zheng, X. M. Yin, J. C. Du, Y. K. Zhao, *J. Hazard. Mater.* **2021**, *416*, 125782–125791.
- [35] M. Guo, J. Q. Lu, Y. N. Wu, Y. J. Wang, M. F. Luo, *Langmuir* **2011**, *27*, 3872–3877.
- [36] I. Tankov, K. Arishtirova, J. M. C. Bueno, S. Damyanova, *Appl. Catal. A* **2014**, *474*, 135–148.
- [37] S. R. Sanivarapu, J. B. Lawrence, G. Sreedhar, *ACS Omega* **2018**, *3*, 6267–6278.
- [38] F. C. Lei, Y. F. Sun, K. T. Liu, S. Gao, L. Liang, B. C. Pan, Y. Xie, *J. Am. Chem. Soc.* **2014**, *136*, 6826–6829.

Manuscript received: October 16, 2023

Revised manuscript received: December 19, 2023

Accepted manuscript online: December 25, 2023

Version of record online: January 3, 2024